Some applications of computerized tomography (CT) in experimental geotechnics

Quelques applications de tomographie automatisé (CT) dans la géotechnique expérimentale

M.C.Alfaro – *Department of Civil Engineering, University of Manitoba, Canada*
R.C.K.Wong – *Department of Civil Engineering, University of Calgary, Canada*

ABSTRACT: The paper presents some applications of CT imaging technologies in geotechnical laboratory testing. CT imaging technique has been used to visualize and characterize fracture features around a simulated borehole within fine-grained soil samples induced by suction and pneumatic pressures. It has also been used to quantify density changes and shear deformations of soil in triaxial compression. In another application, CT has been used to estimate the three-dimensional spatial distribution of porosity, air and water saturations during air-water displacement tests in a soil column. Finally, relationships between air permeability in contaminated soil columns and biodegradation rate of contaminant have been clearly understood with the aid of CT scans. As in other imaging techniques, CT has been found to be a useful tool in analyzing experiments on geotechnical problems.

RÉSUMÉ: Cet article présente quelques applications de techniques d'imagerie de tomographie automatisée pour des essais géotechniques en laboratoire. Cette technique a été employée pour visualiser et caractériser les fractures causés par la succion et par les pressions pneumatiques autour d'un trou de forage simulé dans des échantillons de sol fin. Elle a également été employée pour quantifier les changements de densité et les déformations de cisaillement du sol en compression triaxiale. Dans une autre application, cette technique a été employée pour estimer la distribution spatiale de la porosité, et de la saturation d'air et d'eau pendant des déplacements d'air et d'eau dans une colonne de sol. En conclusion, des rapports entre la perméabilité de l'air dans les colonnes de sol contaminées et le taux de biodégradation d'un contaminant ont été compris à l'aide des balayages de CT. Comme avec les autres techniques d'imagerie, celle - ci s'est avéré un outil utile pour l'analyse de problèmes géotechniques.

1 INTRODUCTION

1.1 *Brief description of CT*

Computerized tomography (CT) is an imaging technique that has been used by the medical community for a number of years. It is a non-destructive analysis that produces an image of the internal structure of a material by reconstruction of attenuation coefficients of x-rays passing through the body. Hence, the technique is widely known as x-ray computerized tomography. As x-rays pass through the object, some are absorbed, some are scattered, and some are transmitted. The radiation transmitted through the object is measured by detectors and referred to as attenuation data. Attenuation is a measure of the reduction in x-ray intensity that results from absorbtion and scattering by the object. The attenuation data is summed over the many different angles from which it was collected using a computer in a method called reconstruction. Reconstruction essentially builds the CT image from the data collected and represents a cross-section of the object. This image contains a matrix of pixels (picture element). Each pixel represents a specific computer tomograph number (CTn). CTn represents the average x-ray attenuation within a volume element, often referred to as a voxel. The size of the voxel is limited by the thickness of the x-ray beam and by the instrument resolution. Relationship between x-ray attenuation and CTn is established by the following equation:

$$CTn = \frac{\mu - \mu_{water}}{\mu_{water}} k \qquad (1)$$

where k is the scaling factor either 500 or 1000; μ and μ_w are the attenuation coefficients of the material and water, respectively.

Adaptation of CT technique for the non-destructive evaluation of geotechnical materials is relatively new. Early applications have been done in petroleum industry to characterize heterogeneity of core samples from hydrocarbon reservoirs (Wellington and Vinegar 1987; Coshell et al. 1994) and to visualize multiphase flow in porous media (Hove et al. 1987; Kantzas et al. 1992). In geotechnical engineering applications, CT imaging technique has been used to quantify and characterize shear deformations and fracture features in soils (Leung et al. 1995; Desrues et al. 1996; Walters et al. 1998; Alshibli et al. 2000; Wong 2000; Otani et al. 2000). In geoenvironmental engineering applications, CT technique has been used to estimate air pattern in soil for air sparging and bioventing (Chen et al. 1996; Wibowo 1996; Maini et al. 1999).

1.2 *Analysis of CT measurement*

Bossi et al. (1990) have shown that the measurement of attenuation from CT is predominantly proportional to the local electron density of the material under consideration. If the material has uniform chemical composition, the measurement is proportional to the local mass density of the object. In effect, CT scanner measures density as a CT number (CTn). Each pixel of a scanned image represents the average density of a voxel at (x,y) cross-section location. The interpretation and analysis of CT data depends on the composition of the volume scanned.

For the case of two-phase geotechnical materials (i.e., solid-air or solid-water system), the average CT number can be defined using the mixture theory (Wong and Wibowo 2000):

$$\chi_{sa}(x,y) = \chi_a \phi(x,y) + \chi_s [1 - \phi(x,y)] \qquad (2)$$

$$\chi_{sw}(x,y) = \chi_w \phi(x,y) + \chi_s [1 - \phi(x,y)] \qquad (3)$$

where χ_a, χ_w, and χ_s are CT numbers of air, water and solid, respectively. The calibrated value of χ_a is –1000 while that of χ_w is 0. The values of $\chi_{sa}(x,y)$ and $\chi_{sw}(x,y)$ are the average CT numbers for solid-air and solid-water at (x,y) location, respectively. The value of $\phi(x,y)$ represents the local porosity at each (x,y) location which can be determined by combining

Equations (2) and (3):

$$\phi(x,y)=\frac{\chi_{sw}(x,y)-\chi_{sa}(x,y)}{\chi_w-\chi_a} \tag{4}$$

For the case of three-phase geotechnical materials (i.e., solid-air-water system), the average CT number at location (x,y) is given as:

$$\chi(x,y)=\chi_a\phi(x,y)S_a+\chi_w\phi(x,y)S_w + \chi_a\phi(x,y)+\chi_s[1-\phi(x,y)] \tag{5}$$

where S_a is the air saturation ($S_a = \phi(1 - S_w)$); S_w is the water saturation, and χ is the CT number for the scanned voxel.

Combining Equations (2), (3), and (5), the air saturation at any (x,y) location can be estimated from:

$$S_a(x,y)=\frac{\chi_{sw}(x,y)-\chi(x,y)}{\chi_{sw}(x,y)-\chi_{sa}(x,y)} \tag{6}$$

It can be seen that the estimation of spatial distributions of porosity and air saturation requires determination of CT data for $S_w = 0$ and 100%.

The porosity $\phi(x,y)$ defined in Equation (4) is the volume of void divided by the volume of a voxel. For the type of CT scanner used in the experiments reported in this paper, the volume of a voxel is 0.75 x 0.75 x 3 mm^3. If the voxel contains more than 8 grains of average diameter of the soil, the calculated porosity is independent of the sampling size because the largest number of grains in the loosest cubic packing is 8. When the soil specimen contains gravel or pebbles larger than a pixel size, the use of Equations (4) and (6) must be treated with caution. Note that the CT number for pebbles is close to that of solid. In this case, the numerator and denominator in Equations (4) and (6) becomes zero, and the calculated porosity or air saturation value becomes undefined.

2 SOIL FRACTURING TESTS

2.1 *Experimental Details*

Experimental studies were conducted to investigate the feasibility of inducing fractures in a soil matrix around a borehole by applying cyclic suction pressures. The theoretical concept involved in this process is the collapse of the soil matrix into a borehole due to the application of zero absolute pressure within the borehole. The collapsed soil matrix would then initiate a zone of dilation around the borehole, thus increasing the porosity and the in-situ permeability around the borehole. The purpose of soil fracturing is to enhance in-situ bioremediation technologies in tight formations such as glacial tills.

Two types of soil specimens were used in the fracture tests. The first soil specimen was prepared from natural silty sand and the second soil specimen was prepared from kaolinite clay. The apparatus used was a modified triaxial cell designed to provide access to the bottom of the soil specimen while under an applied confining pressure (Fig. 1). Details of the soil specimen preparations and testing procedures can be found elsewhere (Wibowo 1996; Alfaro and Wong 1997). A vacuum pump and a Marsh vacuum gauge was used to provide cyclic suction pressures inducing collapse of the soil into the borehole. A maximum gauge pressure of -100 kPa was applied in short time intervals of 30 seconds. During this process, the soil specimen is subjected to a confining pressure of 100 kPa for kaolinite clay specimen and 500 kPa for silty sand specimen in addition to the negative borehole pressure. At the end of the fi ure tests, CT scans of each soil specimen were performed to determine any changes in density.

2.2 *Results and Discussions*

As implied earlier, attenuation coefficient is directly proportional to the mass density. Figure 2 shows three of the six CT images (slices) of the silty sand specimen. Slice 1 was taken near the bottom and slices 3 and 6 were taken near the middle and top of the specimen, respectively. It is interesting to note that the fracture matrix developed in three principal radial directions spaced almost equally around the borehole. A tensile induced fracture can be seen to appear at the tip of one of these fractures (Slice 3) before extending to the outer perimeter of the specimen (Slice 6). Results of CT scan from kaolinite clay also showed the development of fracture matrix. The extent of fractures induced by suction pressure was found to be four times the radius of the borehole and was considered small. However, it was observed by Wibowo (1996) that the combination of cyclic suction and pneumatic fracturing is more effective in creating the desired soil fractures. Suction pressure initiates fractures around a borehole while pneumatic pressure help propagate fractures away from the borehole. Alfaro and Wong (2001) have demonstrated that propagation of fractures with initial fractures or slots (that may be created by suction pressures) required lesser pneumatic pressure compared to that without initial fractures.

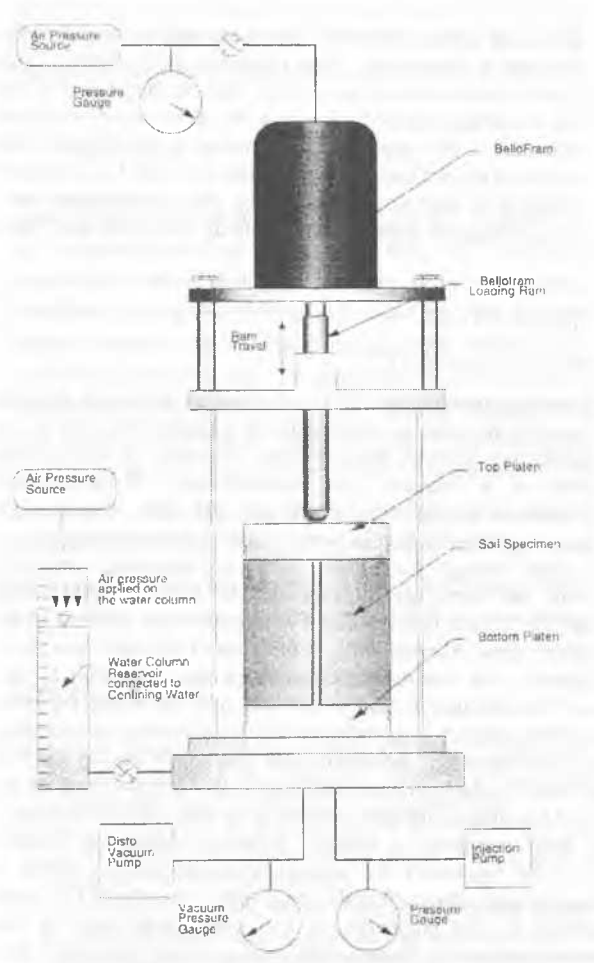

Figure 1. Fracture test setup (after Alfaro and Wong 1997)

(a) Slice 1 (b) Slice 3 (c) Slice 6

Figure 2. CT images of silty sand specimen after suction fracturing

3 TRIAXIAL COMPRESSION TESTS

3.1 *Experimental Details*

CT imaging technique was used to examine the internal deformation of Athabasca oil sand specimens sheared in drained triaxial compression. The Athabasca oil sand is one of the largest oil sand deposits in northern Alberta, Canada. Bitumen is being extracted from the Athabasca oil sand ores using surface mining or steam stimulation methods depending on the buried depth. Athabasca oil sand is a very dense granular material with interlocking fabric. The main mineral composition is dominated by quartz. The in-situ porosity varies from 32 to 35%. Because oil sands are dense uncemented sands, the resulting deformation induced during the recovery process could be excessive and detrimental to surface mining and subsurface facilities. Analyses of these deformation-related problems require geotechnical properties of the oil sand formation that must be evaluated experimentally.

Previous studies on strength and deformability of Athabasca oil sands were determined from conventional stress-strain relationships without considering the internal shearing deformations. Consideration of the internal shearing deformations is important since single and multiple shear bands were observed in the sheared specimen in triaxial compression tests depending on the test boundary conditions. Experiments were performed to study the internal shearing deformations that occurred in triaxial compression tests at low effective stresses. The spatial distributions of porosity within the sheared specimens were studied using the CT imaging technique. Details of the testing program and results can be found in Wong (2000).

3.2 *Results and Discussions*

Table 1 tabulates some physical properties of all specimens. The average water and bitumen saturations are about 13% and 87%, respectively. The initial bulk density is about 20.0 kN/m^3. The final porosity of each specimen was determined using the Dean-Stark distillation extraction method. This method determines the fluid content from the distillation extraction and the solid content by the gravimetric measurement.

Figures 3 and 4 show the images of sheared specimens under the confining stresses of 20 kPa and 600 kPa, respectively. In these figures, the first slice is near the top while the last slice is near the bottom of the specimen. The light colored portions represent volumes of lesser density or dilated portions. Generally, two forms of shear banding were identified: 1) conical and radial shear bands, and 2) multiple and diffused shear bands. Shear bands in a conical shape were observed in the low confining stresses (5 kPa and 20 kPa). Multiple shear bands were observed in higher confining stresses.

The shear band orientations with respect to the horizontal plane and their average thickness are summarized in Table 1 together with the volume of soil specimen subjected to shear banding. There seems to be no clear indication that the orientation of shear band is a function of the confining stress, which is inconsistent with the results observed in plane strain biaxial compression tests on dry coarse sand (Han and Drescher 1993). This descripancy may be attributed to the strong sensitivity of the orientation of shear band with testing conditions, confining stress, material imperfections, and specimen geometry. The average thickness of distinct shear bands at the end of triaxial compression tests estimated from CT images was about 1.4 mm or eight times the mean grain size (d_{50} of the soil used = 0.17 mm) at confining stresses ranging from 100 to 750 kPa. These results are consistent with those observed by other investigators (Scarpelli and Wood 1982; Muhlhaus and Vardoulakis 1987) where shear bands were reported to have thickness of about eight to ten times the mean grain size. The thickness of the shear bands was found to increase significantly when the confining stress drops below 100 kPa. The average thickness of shear bands observed in test under 5 kPa confining stress was about 13 times the mean grain size. This larger thickness may be due to the fact that some grains deform in interlocked groups, such that, the mean diameter of the group is larger than that of individual grains. As for the percentage of volume subjected to shear banding, the shear bands form about 16-47% of the specimen volume. However, there seems to be no trend that the degree of shear band formation is dependent on the confining stress.

It was shown by Wong (2000) that the porosity distribution inside the shear bands can be assumed to be fairly uniform upon reaching a limiting critical value. This limiting porosity is the critical porosity defined by Schofield and Wroth (1968). Samieh and Wong (1995) conducted a series of drain triaxial compression and direct shear tests on reconstituted loose oil-free Athabasca oil sand specimens and found the critical porosity as a function of confining stress as shown in Fig. 5. The confining stress used in Fig. 5 is related to the major and minor principal stresses using the transformation technique assuming that the angle of obliquity is equal to 30 degrees. Also plotted in Fig. 5 are the results of critical porosities estimated from CT images. It can be seen that the limiting porosity inside the shear band follows the trend from global measurements. However, the local measurements of limiting porosity based on CT imaging technique are not exactly the same as those from global measurements of critical porosities. These observations are consistent with the results of Desrues et al. (1996). With these observations, it is evident that the state of soil exhibiting localized shear deformations can be more correctly evaluated by studying the localized zones rather than by global measurements of specimen response. CT imaging technique can be a very valuable tool in studying shear banding and thus enhancing the stress-strain models for soils with localized shear deformations. It may be of importance to capture the evolution of shear band and porosity changes during triaxial compression, such that CT scanning the specimen at various axial deformations (Harris et al. 1995). Research is now underway at the University of Calgary to study the evolution of spatial porosity distribution at any stage of triaxial loading. A special triaxial testing system has been developed to accommodate such innovative and unique triaxial test setup (Thomson and Wong 1999).

4 AIR-WATER DISPLACEMENT TESTS

4.1 *Experimental Details*

Experiments were done to study the air and water flow patterns in soil columns. The results were interpreted with the aid of CT images that provided spatial distributions of porosity, air, and water saturations in the soil. The soil used was a silty sand with fine content (passing No. 200 or 0.075 mm sieve) of about 9% by weight. Details of the experimental setup are shown in Fig. 6. The soil specimen was housed within the plexiglass chamber and held between aluminum plates that were held together by threaded Teflon rods. Teflon rods, as opposed to metallic rods,

Table 1. Physical properties and shear deformation characteristics of Athabasca oil sand specimens (after Wong 2000).

Confining stress (kPa)	Porosity		% Volume in shear band	Shear band orientation (°)	Average Shear Band Thickness (mm)
	Avg. (%)	S.D. (%)			
unsheared	36.8	4.1	-	-	-
5	43.9	7.0	24.5	70 - 78	2.68
20	41.2	6.8	25.1	71 - 80	2.57
50	39.0	4.3	46.6	74 - 77	2.22
100	38.1	4.2	39.4	70 - 81	1.55
300	37.7	3.5	21.3	69 - 72	1.77
450	38.0	5.1	15.8	79 - 77	1.34
600	37.2	4.4	18.9	65 - 77	1.15
750	36.5	4.0	22.4	74 - 78	1.74

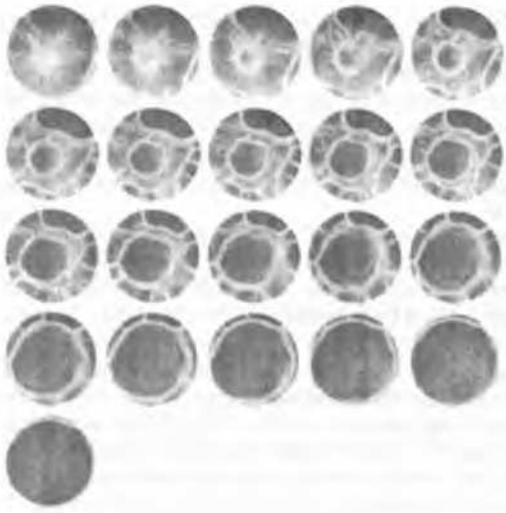

Figure 3. CT images of sheared specimens under 20 kPa confining stress (after Wong 2000)

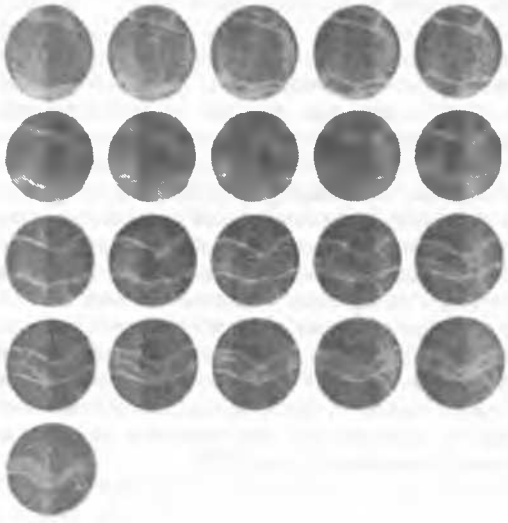

Figure 4. CT images of sheared specimens under 600 kPa confining stress (after Wong 2000)

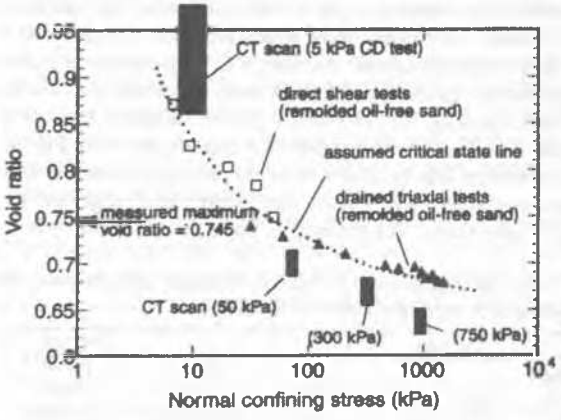

Figure 5. Critical porosity plot (after Wong 2000)

were used to eliminate interference with x-ray beam during CT scanning. The injection pressures and rates of air water were controlled by two separate pressure sources and needle valves. A T-joint connecting the air and water reservoirs was installed to allow mixing of the air and water phases. This arrangement allowed either single-phase injection or two-phase injection into the soil specimen at desired pressures or flow rates. At the downstream end of the cell, a back-pressure regulator was used

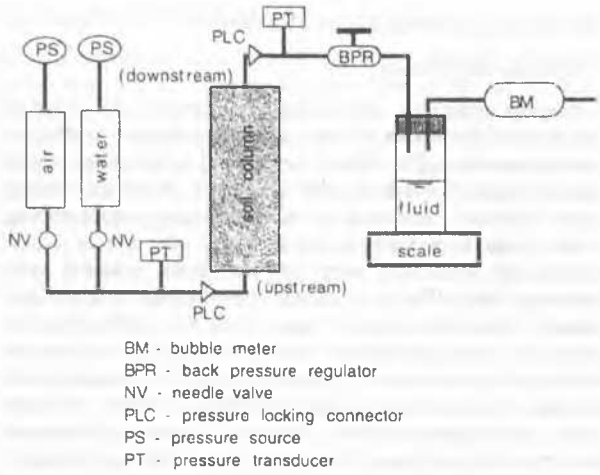

Figure 6. Air-water displacement test set up (after Wong and Wibowo 2000)

to maintain a constant pressure at the outlet end. The air and water were collected at the downstream end. These were separated so that the air volume and the water mass could be measured by a bubble flow meter and a scale, respectively. Pressure transducers were used to monitor the pressures at the upstream and downstream ends of the column cell. Pressure locking connectors were used at both ends of the column cell to maintain pressure inside the cell during the removal of the column cell from the system during CT scanning. CT scanning was done at a dry state ($S_w = 0\%$), close to water saturation ($S_w \approx 100\%$), and at partially saturated conditions.

The main step of this experiment was to inject air and water simultaneously into the specimen at the upstream end under constant pressures of 4 and 10 kPa, respectively. These designed pressures were estimated from the soil-water characteristic curve of the soil based on the grain size distribution data (Fredlund et al. 1998), and they were supposed to yield a water saturation of about 80 to 90%. In this particular step, the back-pressure was open to atmosphere, the air and water flow rates were measured continually until a steady state was achieved. The measured water saturation of the specimen was about 80%. In one test (Test 1), the water was injected at a reduced flow rate. This was controlled by the needle valve connected to the water reservoir at the upstream end of the column cell. After the steady state, the specimen with a measured global water saturation of 71% was scanned at the eight equally spaced marked positions. Global measurements of water saturation were made using gravimetric method. The other test (Test 2) was done in such a way that only air was injected into the specimen to displace all mobile water out of the soil column. The residual water saturation was globally measured to about 61%. The specimen was then scanned at the marked locations. Full description of the testing equipment and procedures are given in Wibowo (1996).

4.2 *Results and Discussions*

Figure 7 shows the spatial distribution of initial porosity at the eight scanned sections together with the porosity histograms. Slice 1 represents the section near the upstream end where air or water was injected into the experimental setup (Fig. 6). Slice 8 represents the section near the downstream end where air or water was collected. It also corresponds to the bottom layer of the soil during compaction in sample preparation. The darker area of the CT image represents lower porosity. Figure 7 shows that there is no distinct high porosity zone distributed around the cell wall, indicating that the smooth rigid plexiglass wall had no effect on the injection test results. There are however few dark spots that can be seen. These are large solid pebbles that were not removed from the specimen preparation. Based on the shape

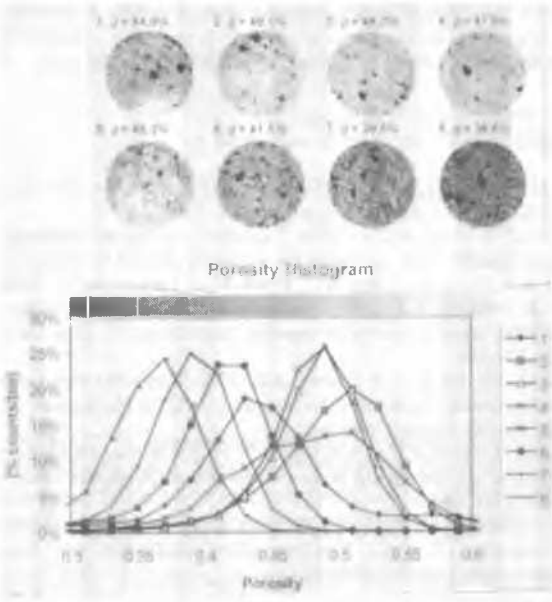

Figure 7. CT images and porosity histograms (after Wong and Wibowo 2000)

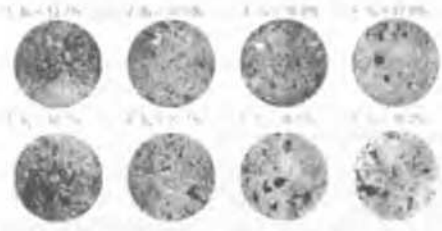

Figure 8. CT images for Test 1 soil column (after Wong and Wibowo 2000)

of porosity histograms and CT images, three types of packing were identified: (I) low average porosity with uniform pattern (Slices 6, 7, and 8; porosity less than 0.40 and standard deviation less than 0.05), (II) high average porosity with uniform pattern (Slices 3 and 4; porosity more than 0.40 and standard deviation less than 0.05), and (III) high average porosity with non-uniform pattern (Slices 1, 2 and 5); porosity larger than 0.40 and standard deviation greater than 0.05; with local low and high porosity spots). This classification was used to interpret the flow patterns observed in the air-water displacement tests of different rates.

Only CT images for Test 1 (S_w = 71%) are given here (Fig. 8). Comparing Figs. 7 and 8 and looking at the positions of big pebbles, it can be reasonably assumed that the air-water injection process did not significantly disturb the soil grain packing or cause a change in local porosity. Local porosities and water saturations were determined using appropriate equations presented in Section 1.2. The average porosities and water saturations estimated from CT imaging technique are quite consistent with the gravimetric method as demonstrated in Table 2. Figure 8 shows again that no air channeling or preferential flow near the cell wall was observed. Small light-colored pixels can be visualized as micro air channels. Type I packing has the largest number and the more uniform distribution of micro air channels. In Type II packing, the total number of micro channels is reduced, but the distribution is also uniform across the section. In Type III packing, the total number of micro air channels is close to that in Type II packing but these are concentrated at localized zones. It was found that the old channels grow in size and new channels are developed around the old ones as the water saturation was reduced from 71 to 61%. At S_w = 61%, the water phase is held by the capillary effect or matrix suction and is no longer mobile. At this irreducible water saturation, some of the micro air channels are connected through the entire soil column establishing a continuous air phase. The airflow behavior of the

Table 2. Comparison of water saturations determined from CT and gravimetric methods (after Wong and Wibowo 2000).

	CT measurements	Gravimetric measurements	Test Condition
Porosity	44.5	42	Initial
Water saturation (%)	77.6	71	Test 1
Water saturation (%)	67.9	61	Test 2

soil column is governed by the configuration of these continuous channels. Global measurements of porosity do not reflect the local characteristics of these micro pores.

It was found by Wong and Wibowo (2000) that there was a general trend of increasing air saturation with decreasing porosity. This observation is inconsistent with the general understanding that high porosity is associated with high air saturation. This understanding may only be valid when applied to multiphase flow in heterogeneous soil media (Chen et al. 1996). Local channeling or fingering has a higher tendency to develop in high porosity areas than in low porosity areas. Isolated airflow patches are preferentially initiated and developed in local high porosity spots. During the air-water displacement, steady state was rapidly achieved in few local spots, resulting in overall low intra-channel or residual air saturations. In uniform low porosity sections, no such distinct local fingering features were observed. The air displacement in low porosity soil is more uniform than that in high porosity soil, and behaves like a plug or piston flow.

The difference in flow behavior observed in high and low porosity areas has practical implications in soil aeration for bioremediation applications. Air breakthrough happens earlier and faster in local high porosity areas than in low porosity areas. However, the air saturation will not increase monotonically with decreasing porosity. At the extreme condition that is relevant in very low-permeability clayey soils, the breadth of air contact or air retention is significantly reduced due to high capillary pressure. There seems to be a critical porosity value for optimum air saturation developed in a soil medium. This critical value can be estimated by conducting air displacement tests on different soils of varying porosities.

5 AIR PERMEABILITY TESTS

5.1 *Experimental Details*

An experimental study was undertaken to determine the rate of biodegradation of hydrocarbon in the soil under cold temperature (5°C). The experimental design consisted of 14 soil columns (similar to the one used in Section 4), 12 of which were contaminated with 2% crude oil. Each soil column was purged with breathing quality air at a flow rate of 4 ml/min. Off-gas samples for each column were analyzed using gas chromatograph (GC) in order to determine CO_2 production rates. Details of the test setup (shown in Fig. 9) and procedures can be found in (Gibb 1999). As a part of Gibb's study, air permeability tests on unsaturated soil columns were conducted. In these tests, an ultra-low pressure transducer was connected to measure the pressure drop between the inlet and outlet of each column. A flow of about 4 ml/min was used for each column. After the columns were connected to the transducer, an interval of 15 minutes was allowed for stabilization before reading was taken. The readings were then converted into inches of water. After a series of calculations, this data was converted into air permeability. Difficulties arose in interpreting the relationships between the biodegradation rate and air permeability. So it was decided to use CT scan images to help in interpreting air permeability and biodegradation measurements.

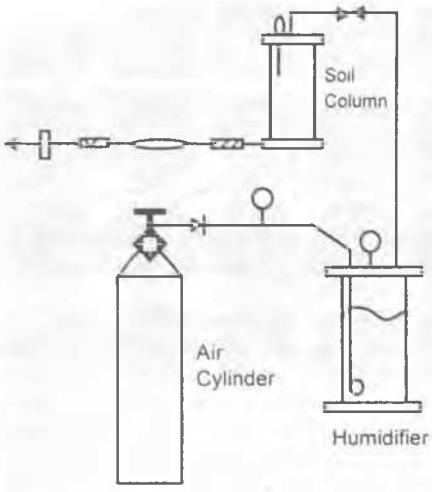

Figure 9. Experimental setup for bioventing test (after Gibb 1999)

Figure 10. CT images of hydrocarbon-contaminated soil columns (after Maini et al. 1999)

5.2 *Results and Discussions*

Figure 10 shows the CT images of two of the soil columns. It is obvious that there are channeling inside the columns due to fractures and cracks. However, the presence of fractures alone did not necessarily resulted to higher air permeability. CT scan data was analyzed (Maini et al. 1999) to find the correlation between the air permeability and the CT numbers and then the correlation between biodegradation and air permeability. To do this, the air permeability was plotted against the average CT number, the standard deviation, the percentage below average, and the percentage below 530 (CT number that corresponds to the maximum void ratio). It was found that air permeability only have good correlation with the percentage below average. This implies that the higher percentage of pore volume below the average pore volume of the entire column resulted in higher permeability. It was also found that the more uniform soil columns have higher permeability compared to the less uniform soil columns. Good correlation was found between the percentage below average and the biodegradation rate of hydrocarbon in the soil column.

6 CONCLUDING REMARKS

Computerized tomography (CT) imaging technique was used to visualize and characterize fracture features around a simulated borehole in fined-grained soils and to examine the internal shear deformations and density changes of oil sand specimens sheared in drained triaxial compression tests. The technique has also been used to visualize and quantify porosity, air and water saturations and to study the multiphase flow patterns in soils. It was also employed in the interpretation of air permeability and biodegradation measurements in bioventing tests on contaminated soils. In a variety of applications reported in this paper, it has been demonstrated that CT is a powerful non-destructive and non-invasive tool in experimental geotechnics. CT will have an important role for studying geotechnical material behavior at micro-structural level, particularly in developing constitutive models for shear deformations and flow patterns in soils.

REFERENCES

Alfaro, M.C. & Wong, R.C.K. 1997. Fracturing in soil. *Research Report No. CE97-1.* University of Calgary, Alberta, Canada.

Alfaro, M.C. & Wong, R.C.K. 2001. Laboratory studies on fracturing of low-permeability soils. *Canadian Geotechnical Journal* (in press).

Alshibli, K.A., Sture, S., Costes, N.C., Frank, M.L., Lankton, M.R., Batiste, S.N. & Swanson, R.A. 2000. Assessment of localized deformations in sand using x-ray computed tomography. *Geotechnical Testing Journal* 23(3): 274-299.

Bossi, R.H., Friddel, K.D. & Lowrey, A.R. 1990. Computed tomography. *Non-Destructive Testing of Fibre-Reinforced Plastic Composites,* New York, Elsevier Applied Science.

Chen, M.R., Hinkley, R.E. & Killough, J.E. 1996. Computed tomography imaging of air sparging in porous media. *Water Resources Research* 32(10): 31013-3024.

Coshell, L., McIver, R.G. & Chang, R. 1994. X-ray computed tomography of Australian oil shales: Non-destructive visualization and density determination. *Fuel* 73(8): 1317-1321.

Desrues, J. Chambon, R., Mokni, M. & Mazerole F. 1996. Void ratio evolution inside shear bands in triaxial sand specimens studied by computer tomography. *Geotechnique* 46(3): 529-546.

Fredlund, D.G., Xing, A. & Huang, S. 1998. Predicting permeability function for unsaturated soil by the soil-water characteristic curve. *Canadian Geotechnical Journal* 35(3): 533-546.

Gibb, A. 1999. *Bioremediation of crude oil in cold climates.* M.Sc. thesis, University of Calgary, Alberta, Canada.

Han, C. & Drescher, A. 1993. Shear bands in biaxial tests on dry coarse sand. *Soil and Foundations* 33(1): 118-132.

Harris, W.W., Viggiani, G. Mooney, M.A. & Finno, R.J. 1995. Use of stereophotogrammetry to analyze the development of shear bands in sands. *Geotechnical Testing Journal* 18(4): 405-420.

Hove, A.O., Ringen, J.K. & Read, P.A. 1987. Visualization in laboratory corefloods with the aid of computerized tomography of x-rays. *SPE Reservoir Engineering* 2(2): 148-154.

Kantzas, A., Marentette, D.F. & Jha, K.N. 1992. Computer-assisted tomography:From qualitative visualization to quantitative core analysis. *Journal of Canadian Petroleum Technology* 31(9): 48-56.

Leung, K.S., Kry, P.R. & Wong, R.C.K. 1995. Visualization of deformation in unconsolidated Athabasca oil sand. *International Heavy Oil Symposium*, Calgary, Canada, Society of Petroleum Engineers.

Maini, M., Alfaro, M.C. & Wong, R.C.K. 1999. Evaluation of air permeability in unsaturated soil columns by computer tomography. *Research Report No. CE99-2.* University of Calgary, Alberta, Canada.

Muhlhaus, H.B. & Vardoulakis, I. 1987. The thickness of shear bands in granular materials. *Geotechnique* 37(2): 271-283.

Otani, J., Mukuniki, T. & Obara, Y. 2000. Application of x-ray CT method for characterization of failure in soils. *Soils and Foundations* 40(2): 111-118.

Samieh, A.M. & Wong, R.C.K. 1995. Assessment of critical state characteristics and the homogeneous response of oil sand at low confining stress. *48th Canadian Geotechnical Conference*, Vancouver, Canada, Canadian Geotechnical Society.

Scarpelli, G. & Wood, D.M. 1982. Experimental observation of shear band pattern in direct shear tests. *IUTM Conference on Deformation and Failure of Granular Materials*, Delft, The Netherlands.

Schofield, A.N. & Worth, C.P. 1968. *Critical state soil mechanics.* McGraw Hill, London.

Thomson, P.R. & Wong, R.C.K. 1999. Design of a triaxial cell for computer tomography scan. *52nd Canadian Geotechnical Conference*, Regina, Canada, Canadain Geotechnical Society.

Walters, D.A., Wong, R.C.K. & Kantzas, A. 1998. The application of computer-assisted tomography in the analysis of fracture geometry. *Geotechnical Testing Journal* 21(4): 328-335.

Wellington, S.L. & Vinegar, H.J., 1987. X-ray computerized tomography. *Journal of Petroleum Technology* 39(8): 885-898.

Wibowo, R. 1996. *Bioremediation and fracturing in soil.* M.Sc. thesis, University of Calgary, Alberta, Canada.

Wong, R.C.K. 2000. Shear deformation of locked sand in triaxial compression. *Geotechnical Testing Journal* 23(2): 158-170.

Wong, R.C.K. & Wibowo, R. 2000. Tomographic evaluation of air and water flow patterns in soil column. *Geotechnical testing Journal* 23(4): 413-422.